Article

Spectroscopic fingerprints of iron-coordinated cobalt and iron porphyrin layers on graphene

Francesco Armillotta, Davide Bidoggia, Pietro Biasin, ..., Luca Floreano, Maria Peressi, Erik Vesselli

evesselli@units.it

Highlights

A 2D metal-organic framework is self-assembled on a single graphene sheet

Single metal atoms yield mono- and bimetallic homo- and heterostructures

Coordination occurs both at terminal pyridinic N sites and at the macrocycle

The metal-organic framework is an optimal prototype for 2D electrocatalytic materials

Here, Armillotta et al. develop a 2D metal-organic framework supported on a single graphene sheet by exploiting tetra-pyridyl porphyrins as molecular tectons. Iron and cobalt single-metal-atom sites are stabilized to yield mono- and bimetallic homo- and heterostructures, ultimately demonstrating a self-assembled heterostructure that may be an optimal candidate for prototype (photo)(electro) catalytic materials.

Article

Spectroscopic fingerprints of iron-coordinated cobalt and iron porphyrin layers on graphene

Francesco Armillotta,[1,5] Davide Bidoggia,[1] Pietro Biasin,[1] Antonio Annese,[1] Albano Cossaro,[2,3] Alberto Verdini,[2] Luca Floreano,[2] Maria Peressi,[1] and Erik Vesselli[1,2,4,6,*]

SUMMARY

Achieving control in the design of monolayer 2D functional catalysts represents a significant challenge. If that challenge is surmounted, coordinated single-metal-atom sites can offer tailored electronic configuration, ligation geometries, chemical activity and selectivity, and stability. We report spectroscopic evidence of the formation of a 2D metal-organic framework supported by a single graphene sheet in which coordination among tetra-pyridyl porphyrins (TPyPs) is spontaneously obtained by exploiting single iron atoms. The spectroscopic characterization, together with *ab initio* methods, reveals that metal intermolecular coordination occurs via the terminal nitrogen atoms in the pyridinic residues of adjacent TPyPs. Interestingly, the peripheral coordination of metal atoms impacts the electronic configuration of the porphyrin's core. Due to the chemical stability of the graphene layer, its weak interaction with the metal-organic framework, and the known electrochemical activity of the latter, this system represents an optimal candidate for the design and engineering of prototype 2D electrocatalytic materials.

INTRODUCTION

Catalysts play a major role in the synthesis of chemical and energy vectors and are of utmost importance for the ongoing energy transition.[1,2] For metal-based single-atom catalysts (SACs), the active sites consist of isolated single atoms stabilized by a supporting template, or by alloying with another metal,[3,4] or by embedding in 2D or 3D metal-organic frameworks (MOFs) in a surface coordination chemistry picture.[5] SACs are attracting increasing interest for multiple reasons. While from an economic and ecological point of view, they optimize the active metal quantity, more importantly, they allow for a local tuning of the electronic and geometric configurations for best performance and selectivity. The decrease in size is accompanied by the takeover of quantum-size effects, which, together with the low coordination environment and the metal-support interaction, can be exploited to tailor the specific activity.[6–8] Finally, from a fundamental perspective, they represent a model system for heterogeneous catalysis, with well-defined and identical active sites.

Recently, 2D MOFs based on self-assembled tetra-pyridyl porphyrins (TPyPs) have attracted attention due to their interesting oxygen reduction/oxygen evolution reaction (ORR/OER) electrocatalytic (EC) activity and stability on a gold substrate.[9,10] Indeed, due to the presence of meso-substituted pyridyl residues, these molecules can easily host extra-molecular tetra-coordinated single-transition metal species if co-deposited on a sufficiently weakly interacting substrate upon mild annealing or

[1]Department of Physics, University of Trieste, via A. Valerio 2, 34127 Trieste, Italy

[2]CNR-IOM, Area Science Park, S.S. 14 km 163.5, 34149 Basovizza, Trieste, Italy

[3]Department of Chemical and Pharmaceutical Sciences, University of Trieste, via L. Giorgieri 1, 34127 Trieste, Italy

[4]Center for Energy, Environment and Transport Giacomo Ciamician, University of Trieste, Trieste, Italy

[5]Present address: Institute of Physics Ecole Polytechnique Fédérale de Lausanne (EPFL) Station 3, Lausanne 1015, Switzerland
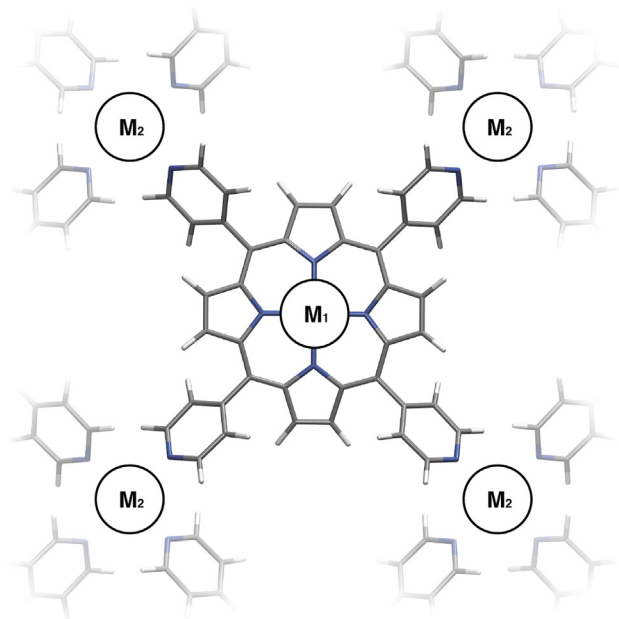
[6]Lead contact

*Correspondence: evesselli@units.it

https://doi.org/10.1016/j.xcrp.2023.101378

Figure 1. Schematic chemical structure
Structure of the metal 5,10,15,20-tetra(4-pyridyl)-21H,23H porphyrine (M_1TPyP) and model of the M_1TPyPM_2 extended bimetallic catalyst upon metal atom (M_2) physical vapor deposition (M_1 = Co, Fe; M_2 = Fe).

even at room temperature.[10–12] Remarkably, Wurster et al.[9] reported an 80-fold increase of the ORR activity passing from the monometallic M_1TPyP/Au(111) (M_1 = Co, Fe) monolayers to the bimetallic M_1TPyPM_2 ($M_{1,2}$ = Co, Fe) combinations, where the additional metal atom M_2 is tetra-coordinated to the pyridyl residues (see Figure 1). The increased EC performance cannot be simply attributed to the number of the active sites but, rather, must find its origin in a deep change of the MOF intrinsic electronic structure, such as, for instance, the nature of the metal species embedded in the MOF and the mutual interactions between the different ad-species.[9,13] For this purpose, it is useful to decouple the layer from the substrate to study its intrinsic properties independently from substrate contributions. The latter can indeed affect the geometry of the layer[14,15] and its chemical reactivity via the surface *trans* effect through competing charge transfer mechanisms in the picture of what is also addressed as the fifth ligand at the single-metal-atom site embedded in the macrocycle.[16–18] Moreover, the weakening of the molecule-substrate interaction favors the role of the tectons' lateral coupling, yielding the growth of ordered layers according to the molecular shape and functional groups instead of that being mostly driven by the substrate's geometry. Charge delocalization for the coherent excitonic singlet fission between adjacent centers, energy funneling, or efficient charge conductivity can so be observed.[19] For this purpose, almost free-standing graphene (Gr) on Ir(111) represents an ideal substrate choice due to the presence of weak van der Waals forces[16,20]; the excellent chemical passivation (e.g., ideal for near-ambient pressure experiments)[21]; the high mobility of the adsorbed species, which possibly reflects in a more effective MOF self-assembly; and the possibility of reversible doping.[22]

In this article, we report a detailed X-ray photoelectron spectroscopy (XPS) and near-edge X-ray absorption fine structure (NEXAFS) analysis of the CoTPyP, FeTPyP,

p-pol

s-pol

A

Data
Fit
Iminic $1s \Rightarrow \pi^*$
Pyridinic $1s \Rightarrow \pi^*$
$1s \Rightarrow \sigma^*$
Fermi Level
Ionization step
Rydberg states

CoTPyP/Gr/Ir(111)

B

A DFT

DFT $N_{macrocycle}$
DFT $N_{pyridinic}$

CoTPyP/Gr/Ir(111)

B DFT

C

FeTPyP/Gr/Ir(111)

D

E

CoTPyPFe/Gr/Ir(111)

F

G

FeTPyPFe/Gr/Ir(111)

H

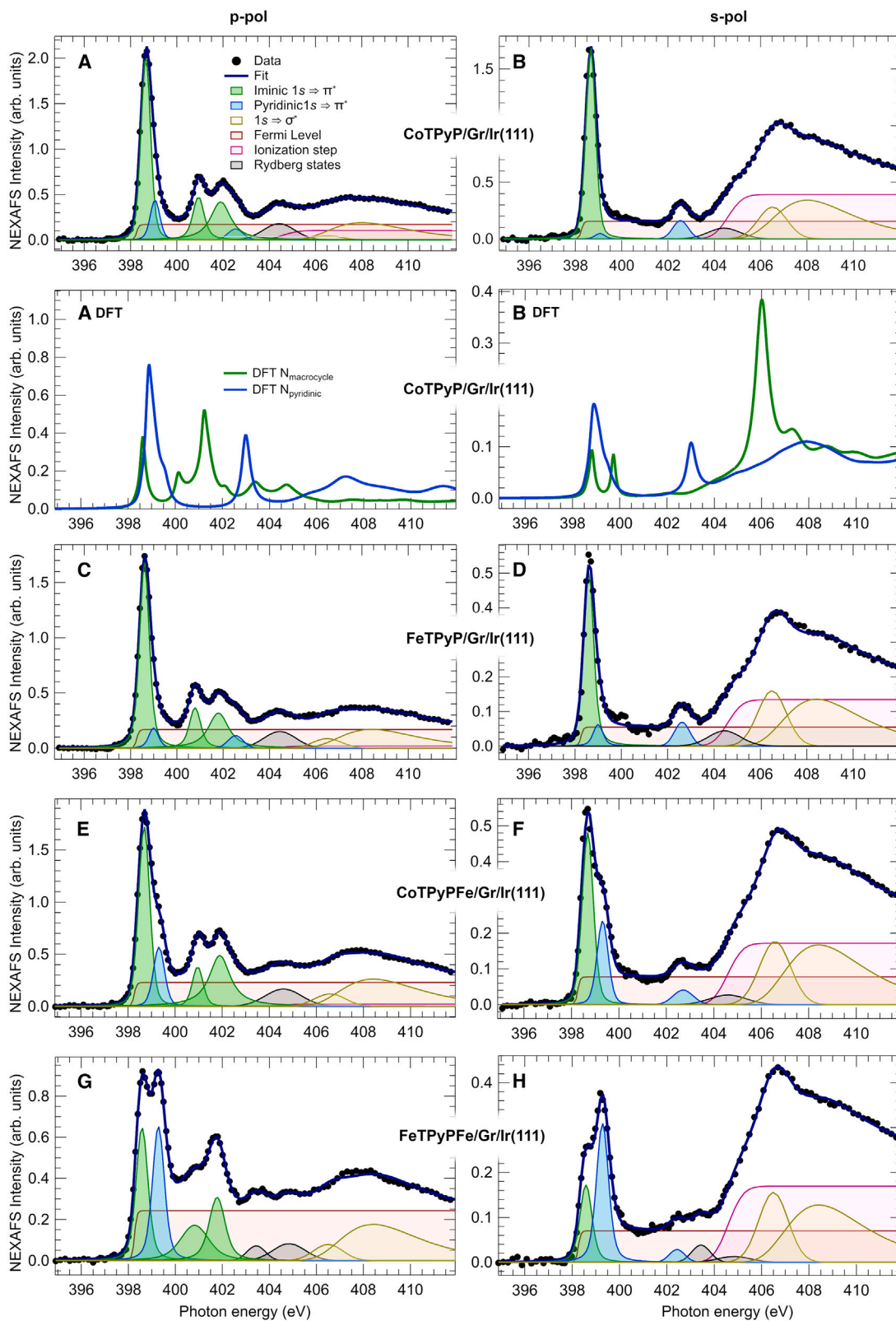Photon energy (eV)

Photon energy (eV)

Figure 2. N 1s edge NEXAFS spectra

(A–H) Experimental spectra (dotted curves) together with their fit function (solid lines) and deconvolutions (filled profiles) for (A) CoTPyP p-pol; (B) CoTPyP s-pol; (C) FeTpyP p-pol; (D) FeTPyP s-pol; (E) CoTPyPFe p-pol; (F) CoTPyPFe s-pol; (G) FeTpyPFe p-pol; and (H) FeTpyPFe s-pol. Simulated adsorption spectra for iminic (green) and pyridinic (blue) N atoms are plotted in (A^{DFT}) CoTPyP p-pol and (B^{DFT}) CoTPyP s-pol.

CoTPyPFe, and FeTPyPFe monolayers grown in ultra-high vacuum (UHV) conditions on Gr/Ir(111) by physical vapor deposition. We show the multiple spectroscopic fingerprints of the bond formation between the pyridinic nitrogen atoms ($N_{pyridinic}$) and the post-evaporated single iron atoms, supported by *ab initio* density functional theory (DFT), thus providing evidence of the transition from a molecular layer to a MOF. For this purpose, the N 1s core level and the absorption edge are used as primary fingerprints. The analysis of the measured Co and Fe $2p_{3/2}$ core levels in terms of binding energy (BE) shift and multiplet splitting structure remodulation proves the interaction between the metal species inside and outside the macrocycle. For the homobimetallic layers, the two metal atom sites are electronically non-equivalent. The thermal stability of the monometallic CoTPyP and FeTPyP layers has also been investigated, showing that the porphyrins are stable up to 550 K; at higher temperatures, competing desorption and degradation processes set in.

RESULTS AND DISCUSSION

Spectroscopic characterization of the layers with N-edge NEXAFS

Since terminal nitrogen species are an optimal benchmark to prove coordination of the Fe metal atoms to the pyridinic groups, we will first focus on the N absorption edge. Figures 2A–2D show the N 1s edge NEXAFS spectra collected for CoTPyP/Gr/Ir(111) and FeTPyP/Gr/Ir(111), respectively, with the best-fit curves and the corresponding deconvolution profiles, together with the assignment of the spectral components. As introduced above, TPyPs contain four iminic nitrogen atoms that are embedded into the macrocycle and four peripheral pyridinic N in the outermost termination of the residues. This implies that, in a first approximation, we can use a "building block" approach for the assignment of the NEXAFS resonances.[23] For this purpose, we took Fe(II)-tetra phenyl porphyrin (FeTPP) and pyridine molecules as a spectroscopic reference, both previously studied in the literature, since they present exclusively the iminic or the pyridinic nitrogen species, respectively.[24,25] The two resonances at 401.0 (400.8) and 401.9 (401.8) eV in our CoTPyP (FeTPyP) layers, clearly evident in p-pol, well compare with those of FeTPPs.[24] The resonance at 402.5 eV reported for pyridine appears in our spectra of the $M_{1,2}$TPyP layers in s-pol (Figures 2B and 2D) and as a shoulder in p-pol (Figures 2A and 2C). Lastly, the sharp and intense component at 398.5 eV is present in all cases and is thus ascribed to the overlapping contribution from the iminic and pyridinic species. The above-mentioned transitions are all identified as 1s $\rightarrow$ π^*. We fitted the N-edge NEXAFS profiles by using Voigt functions, and, based on the above observations, the two contributions (iminic and pyridinic) at 398.5 eV were constrained to share the same line shape to limit the number of degrees of freedom. As a result, we got the iminic species to be centered at 398.64 (398.58) eV and the pyridinic at 399.04 (398.98) eV for CoTPyP (FeTPyP) layers. In addition to the already discussed transitions at 401.0 and 400.8 (iminic), 401.9 and 401.8 (iminic), and 402.5 eV (pyridinic), the introduction of an additional, broad resonance attributed to unresolved Rydberg states and centered at 404.5 eV (fitted with a Gaussian function) is necessary in order to properly describe the experimental data.

Moving to higher energies, we set at 404.8 eV the initial value for the ionization potential step position, following the literature,[25] before optimizing both its line-shape and energy position for CoTPyP (p-pol). Interestingly, there is a non-vanishing,
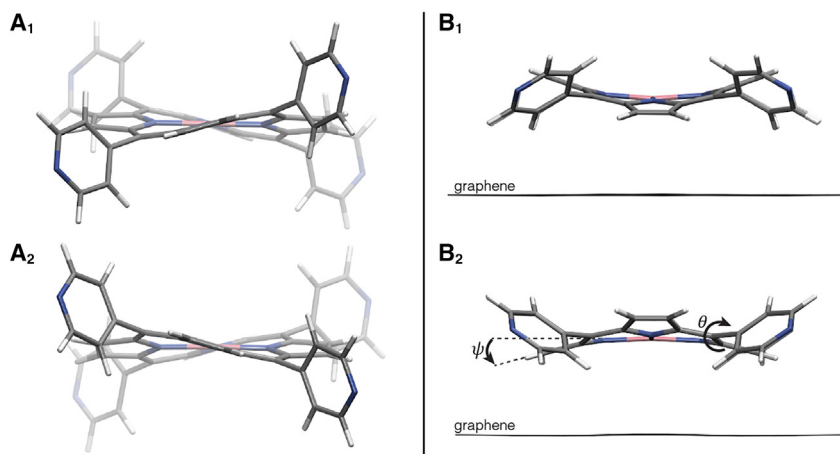
Figure 3. CoTPyP geometry
Lowest energy geometrical structure predicted for a single isolated CoTPyP molecule in the gas phase (A_1 and A_2) and adsorbed on graphene (B_1 and B_2). Two side views (1 and 2) are shown in both cases for best clarity.

non-resonant absorption background in the 400–402 eV energy region (MTPyP s-pol) that can be properly reproduced by the fitting procedure only by adding another step function. This has to be attributed to transitions to a continuum of empty states occurring before ionization, usually observed in the case of molecules electronically coupled to substrate states close to the Fermi level.[23] Therefore, here, a good electronic coupling with the Gr/Ir substrate is likely established through the molecular macrocycle rather than by the central metal atom as on strongly interacting supports. Two π resonances can be finally distinguished at higher photon energies, especially examining the s-polarization spectra. They were both fitted with a Gaussian function, with an asymmetry parameter for the higher energy one, associated with an unresolved vibrational structure. We recall that the data were deconvoluted by best fitting with the sum of the mentioned spectral components convoluted with a 0.2 eV Gaussian function, which takes into account the experimental resolution and the intrinsic broadening due to defects and multiatom spectral contributions.

The molecular adsorption geometry can be inferred by the dichroic behavior of the resonances. We can attribute a tilting angle θ (with respect to the Gr plane) of $36° \pm 4°$ for the pyridyl residues and an angle ψ of $38° \pm 4°$ for the iminic groups on the basis of the observed angular dependence of the resonances in the 399–400 eV range. The resonances centered at about 401 and 402 eV, ascribed likewise to the iminic component, show almost perfect dichroism (see Figures 2A–2D), supporting the planar adsorption geometry of the macrocycle. The residual intensity of the iminic resonances in s-polarization is likely originated by a saddle-shape distortion of the macrocycle rather than by an effective tilting of the surface. This picture is confirmed also by the structural optimization performed in the DFT simulations starting from the periodic molecular arrangement previously observed by Wurster et al. for FeTPyP on gold substrates and shown in Figures SI-S1B of that study.[9] In our case, the predicted adsorption geometry of TPyP molecules (Figures 3B_1 and 3B_2) is found to be a compromise between the interaction with the Gr layer, which forces the pyridinic groups to be as flat as possible, and the steric repulsion between iminic and pyridinic hydrogen atoms. This is made clear by the comparison with the optimized geometry of a CoTPyP molecule in gas phase (Figures 3A_1 and 3A_2), where the interaction with a substrate is absent.

From our calculations, pyridinic groups are rotated in alternated directions by an angle θ in the 38.0° ± 1.5° range with respect to the Gr layer, while the pyrrolic rings in the macrocycle are rotated by just ψ = 18°, forming a saddle shape. This is in agreement with previous observations on similar systems.[26–28] The hypothesis of the adsorption geometry in which the whole macrocycle is inclined with respect to the surface can be therefore ruled out.

Further confirmation of this picture and of the provided experimental peak attribution comes from the *ab initio* simulation of the N 1s adsorption spectra for the CoTPyP layer in p- and s-polarizations (Figures 2A^{DFT} and 2B^{DFT}). As a matter of fact, the π* resonances of both species are superimposed around 398.5 eV; the two resonances at 401 and 402 eV pertain to iminic species and show a complete dichroic behavior, while the resonance at 402.5 eV, associated with pyridinic species, has a partial dichroic character. The agreement with the experimental NEXAFS spectra is thus excellent in both cases.

Following evaporation of the Fe adatoms, the N 1s edge NEXAFS spectra show the most dramatic difference in the 398–400 eV energy region, as it can be seen for the CoTPyPFe (Figures 2E and 2F) and FeTPyPFe (Figures 2G and 2H) monolayers. We can now resolve in both polarizations, and most evidently in the FeTPyPFe case, two π* resonances at 398.66 (398.56) and 399.29 (399.26) eV in the CoTPyPFe (FeTPyPFe) absorption spectra. We ascribe the former to the iminic N 1s → π* transition and the latter to the pyridinic N 1s → π* transition, which undergoes the major shift (+0.3 eV) upon metalation, thus supporting the direct linking of pyridinic nitrogen atoms to the additional iron. On the contrary, the iminic species undergo a fairly observable shift of only 0.02 eV in both systems. The remaining π* and σ* resonances, whose deconvolution parameters were reoptimized for the bimetallic systems, do not show relevant modifications, either in energy or dichroism, indicating that the internal geometry of the porphyrinic plane is hardly affected by the peripheral binding of iron. The fitting parameters of the ionization potential and Fermi level were kept fixed to the pre-deposition values.

Spectroscopic characterization of the layers with N 1s XPS

Figures 4A and 4B shows the N 1s core-level spectra of the CoTPyP/Gr/Ir(111) and FeTPyP/Gr/Ir(111) systems, respectively, with the corresponding deconvolution profiles. The line profiles of the two non-equivalent species of nitrogen atoms are modeled with two Voigt functions, centered at 399.1 (398.94) eV for the pyridinic and 398.82 (398.48) eV for the iminic species in the CoTPyP (FeTPyP) monolayer, according to the literature.[14,20] In order to minimize the number of degrees of freedom, in a first approximation, all components share the same, previously determined,[20] Lorentzian width of 0.27 eV. In addition, a broad feature can be observed at higher binding energy, which is well reproduced by a Gaussian function centered at higher binding energy, at 400.31 eV for CoTPyP and at 399.96 eV for FeTPyP layers. The energy separation from the corresponding iminic peak identifies this spectral feature as a photoelectron energy loss due to the excitation of one electron from an occupied to an unoccupied molecular orbital (shake-up satellite). The best-fitting parameters are reported in Table S1.

Coordination of pyridinic N with Fe atoms yields relevant changes also in the N 1s core level, as shown in Figures 4C and 4D. The fitting strategy consists of starting from the parameters of the corresponding monometallic layer and releasing the amplitudes, the Gaussian widths, and the binding energies of the two core level peaks and the shake-up satellite. The two Voigt peaks, attributed to the iminic and
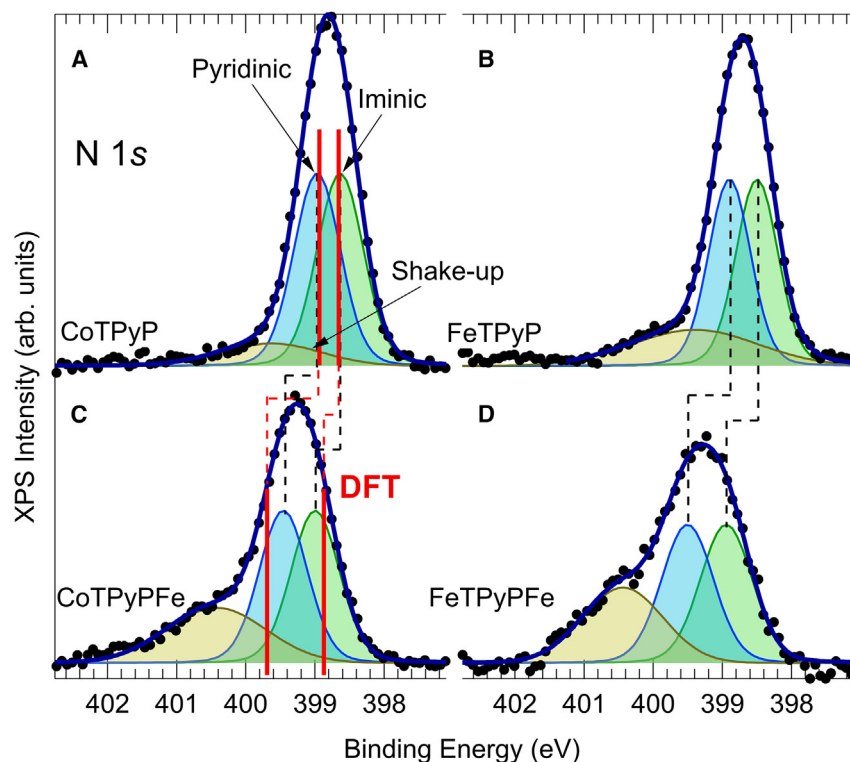
Figure 4. XPS spectra for the N 1s core level

Experimental data (dots) together with their fit function (blue solid lines) and deconvolution (filled profiles). The red lines indicate the DFT prediction for the relative CLSs of the two N species (note that the absolute position is arbitrary). The corresponding samples are labeled in the figure.

pyridinic N atoms, share the same amplitude and Gaussian width. According to our interpretation, the contribution attributed to pyridinic N undergoes a chemical shift of +330 (+550) meV in the case of CoTPyPFe (FeTPyPFe) due to direct binding to elemental iron. A relevant chemical shift is observed also for the peak associated with the iminic N species, +210 meV for CoTPyPFe and +470 meV for FeTPyPFe. This indicates that the electronic configuration of the macrocycle is also affected upon formation of the MOF, inducing an almost rigid shift of the levels since the NEXAFS transitions remain almost unaffected. The Gaussian width slightly changes upon metalation, showing an inverse trend between CoTPyPFe (decreasing from 0.74 ± 0.01 to 0.62 ± 0.02 eV) and FeTpyPFe (increasing from 0.61 ± 0.02 to 0.74 ± 0.04 eV). Our DFT calculations predict the same binding energy hierarchy of the pyridinic and iminic N 1s core levels in all cases, with a relative separation of Δ (N 1s)$_{CLS}$ = 0.28 eV in CoTPyP, which increases to 0.82 eV in the case of CoTPyPFe, in excellent agreement with our experimental data and interpretation. Considering the coordination numbers, in principle, Fe ad-atoms may coordinate 4, 3, 2, or down to single porphyrins. Nevertheless, the relative porphyrin to Fe ad-atom coverage and the shift of the N 1s components support coordination of all peripheral N atoms in a single, prevailing geometry, yielding 4-fold symmetry as the most compatible, thus anticipating confirmation by scanning tunneling microscopy imaging.

Finally, additional evidence of the direct Fe-N binding resides in the remarkable growth of the shake-up weight in the N 1s spectra, associated with access to novel
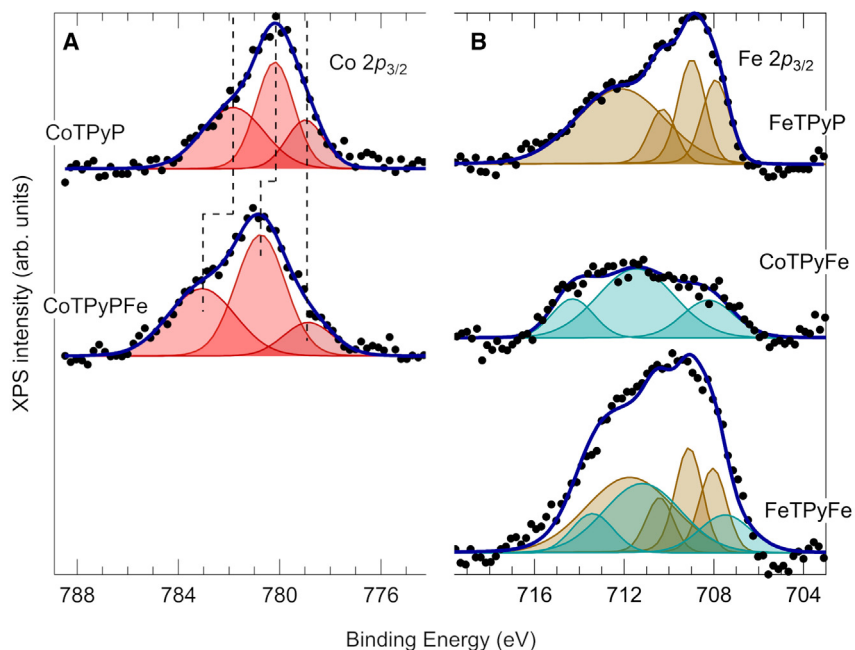
Figure 5. XPS spectra of Co 2$p_{3/2}$ and Fe 2$p_{3/2}$

(A and B) Experimental data for the (A) Co 2$p_{3/2}$ and (B) Fe 2$p_{3/2}$ core levels (dotted curves) together with their fit function (blue solid lines) and deconvolutions (filled profiles) for all M$_1$TPyPM$_2$ combinations with 1 = Co, Fe, and 2 = empty, Fe.

relaxation channels thanks to the formation of new states.[26] The amplitude of the broad shake-up resonance almost triples in CoTPyPFe (from 0.21 $\pm$ 0.01 to 0.53 $\pm$ 0.02) and quintuples in FeTpyPFe (from 0.06 $\pm$ 0.01 to 0.30 $\pm$ 0.04) upon metalation of the layer.

Spectroscopic characterization of the layers with Co 2p XPS

The Co 2$p_{3/2}$ core level of the CoTPyP monolayer has a complex structure due to the coupling, in the photoemission process, between the 2p core-level hole and the high-spin valence electrons (see Figure 5A, top panel).[20,27,29] The multiplet splitting (MS) structure has been empirically modeled, according to literature, with a Doniach-Šunjić (DS) envelope centered at 780.6 eV and a Gaussian component at 782.2 eV. An additional DS component at 779.4 eV accounts for the Gunnarsson and Schönhammer (GS) transfer of the screening charge.[29,30] Indeed, in the CoTPyP multilayer spectrum (Figure S1) the GS is quenched since the charge transfer from the substrate is suppressed. The best-fitting parameters are reported in Table S2.

The influence of iron deposition on the Co 2$p_{3/2}$ core level is shown in Figure 5A (middle panel). The resonances associated with the MS shift toward higher binding energies, specifically +0.3 eV for the DS component at 780.1 eV and +0.6 eV for the Gaussian component at 782.2 eV. Instead, due to its different origin, the GS resonance position is not affected, while its spectral weight diminishes by 30%, indicating a partial decoupling from the substrate due to the suppression of the electron transfer.[31] The MS component described by the Gaussian shape at 782–783 eV undergoes a broadening from 1.8 to 2.3 eV, witnessing a remodulation of the MS amplitudes, associated with a change of the electronic configuration in the cobalt valence states.

Spectroscopic characterization of the layers with Fe 2*p* XPS

For the description of the complex MS structure of the Fe $2p_{3/2}$ XPS core level in the FeTPyP/Gr/Ir(111) heterostack, a similar argument as for the Co $2p_{3/2}$ analysis has to be taken into account,[32] as reported in Figure 5B (the best-fitting parameters are reported in Table S3). The partially unresolved MS structure is modeled by two DS peaks centered at 708.9 and 710.1 eV and by a broad Gaussian at 712.5 eV, which accounts also for shake-up contributions. Even in this case, the GS screening charge is present, as indicated by the DS at lower binding energy (707.9 eV).

In CoTPyPFe (Figure 5B, middle panel), the Fe $2p_{3/2}$ profile is described by two DS envelopes centered at 711.4 and 714.3 eV, associated with the MS structure, and a third one at 708.2 eV, associated with the GS screening charge, as in the cobalt core-level analysis.

Given the overall complexity of the Fe $2p_{3/2}$ lineshape, we approximated the lineshape of FeTPyPFe (Figure 5B, bottom panel) by adopting a building-block model where the iron core-level profile is a linear combination of the one in FeTPyP (Figure 5B, top panel), where only the iron in the macrocycle is present, and the one in CoTPyPFe (Figure 5B, middle panel), where only the iron bonded to the pyridinic terminations is present. This model assumes a complete decoupling between the metal atoms inside and outside the macrocycle, which we know to be inappropriate in light of the above analysis on both the N 1*s* and Co $2p_{3/2}$ core levels. Nevertheless, as we shall see, the large spectral difference between the Fe $2p_{3/2}$ profiles in FeTPyP and CoTPyPFe encouraged us to use in any case this model as a best compromise and to avoid overfitting.

Thermal stability of the layers

In order to investigate the thermal stability of both CoTPyP/Gr/Ir(111) and FeTPyP/Gr/Ir(111) molecular monolayers, the systems have been stepwise annealed from room temperature (MOF growth temperature in this case) to 970 K. In both sequences (Figure 6), the evolution of the N 1*s* core levels was monitored. In the deconvolution procedure, the Lorentzian width of the pyridinic and iminic contributions to the line profile was kept fixed to the initial value of 0.27 eV, consistent with the previous analysis. Positions and Gaussian width were left instead free to vary.

For CoTPyPs (Figure 6A; best-fitting parameters reported in Table S4), annealing to 470 K induces a chemical shift of +130 meV for the iminic and of +210 meV for the pyridinic nitrogen species, indicating the rearrangement of metastable phases, as already observed in the case of similar TPyPs.[33] The Gaussian width does not change within the error, indicating an irrelevant change in the sample heterogeneity. A further investigation on the local structure, which should be carried out with parallel scanning tunneling microscopy (STM) measurements, is behind the purpose of this article, which is dedicated to spectroscopy. Annealing to 550 K does not induce any further relevant change. Similarly, FeTPyPs (Figure 6B; best-fitting parameters reported in Table S5) exhibit a negligible change of the Gaussian width (from 0.60 ± 0.02 to 0.61 ± 0.03 eV) when annealed to 550 K and a 110 meV binding energy increase of both iminic and pyridinic components.

At higher temperature, the line shape and the relative BE distance of the three peaks were locked, while the absolute BE of the whole envelope was left free to vary. In the CoTPyP/Gr/Ir(111) system (Figure 6A), from 550 K and above, the addition of a Gaussian component at 402 eV was necessary to reproduce the experimental
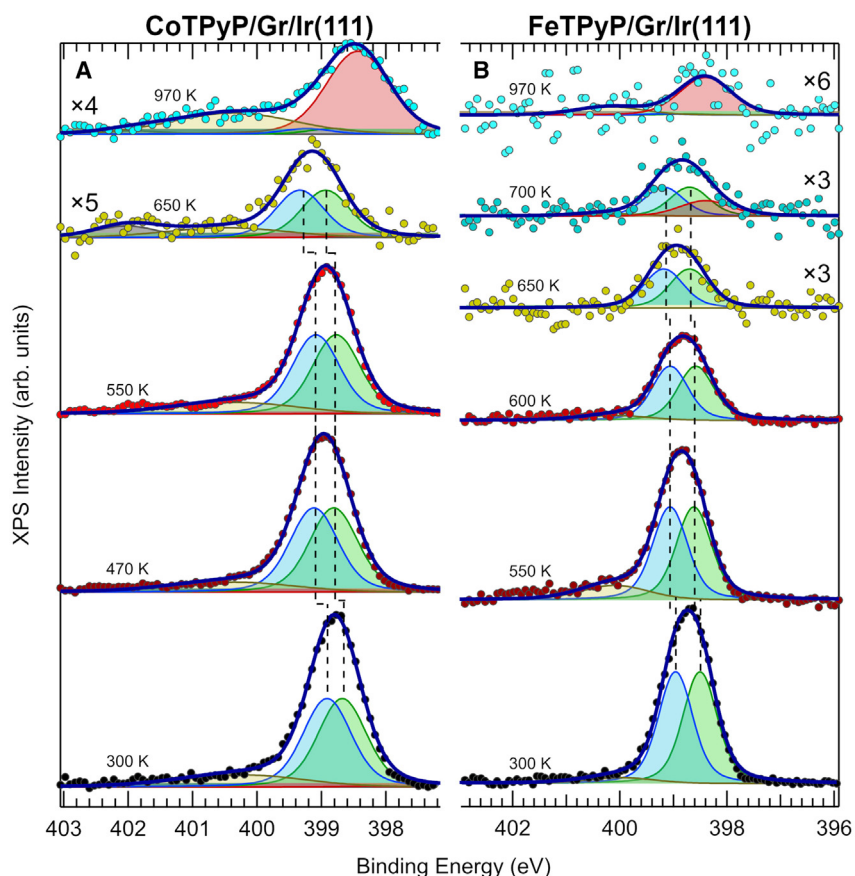
Figure 6. XPS N 1s spectra as function of the annealing temperature
(A and B) XPS N 1s core-level spectra of (A) CoTPyP/Gr/Ir(111) and (B) FeTPyP/Gr/Ir(111) collected at room temperature upon stepwise annealing to the indicated temperature values. The best-fit envelope and the corresponding deconvolution are shown for each spectrum. Filling color legend: green, iminic nitrogen; magenta, pyridinic nitrogen; gray, satellite features.

data, associated with graphitic N atoms (i.e., nitrogen atoms substituting carbon atoms in the Gr honeycomb-like lattice).[34,35] In fact, we decided to fit it with a Gaussian profile in place of a Voigt function due to the low signal-to-noise ratio of the spectra collected at high temperatures, associated with the corresponding lower surface concentration of the species. Indeed, the photoemission intensity drastically decreases with temperature (beyond 550 K) due to the predominant desorption process in competition with molecular decomposition. The occurrence of this latter high binding energy feature can be explained indeed in terms of the decomposition of the CoTPyP molecules. Moreover, at 970 K, a new, Voigt-shaped peak grows at low binding energy (398.27 eV), associated with a strongly substrate-interacting nitrogen species.[27] The same component can be observed also in the FeTPyP series, where it appears at 700 K and is the only one remaining at 970 K, with similar intensity (Figure 6B). Concerning the MOFs, we do not expect significant differences in temperature stability of the layers since decomposition is initially driven by the progressive dehydrogenation of both macrocycle and residues, yielding stronger bonding to the Gr sheet and a precursor to the embedding of N and metal atoms into Gr.

In summary, we have investigated the spectroscopic fingerprint of the mono- and bimetallic (Co,Fe)TPyPFe layers, providing evidence for iron bonding to the pyridinic

nitrogen atoms. For both systems, the N 1s absorption edge spectra show a chemical shift of the on-edge π^* transition of the pyridinic N species, attributed to direct Fe-N linking, in agreement with the corresponding N 1s core-level shifts and DFT simulations. The remarkable increase of the shake-up satellite features in the XPS spectra suggests the formation of additional electronic states, related to the Fe–N$_{pyridinic}$ bonding, participating in the inelastic energy dissipation channels. Besides, the Co and Fe core-level profiles reveal the different electronic configuration of the metal species bonded in the macrocycle or to the peripheral pyridinic residues. Investigation of the thermal stability of the FeTPyP and CoTPyP layers shows good resilience to degradation, with competing desorption and decomposition observed beyond 550 K for both layers.

EXPERIMENTAL PROCEDURES

Resource availability

Lead contact

Further information and requests for resources should be directed to and will be fulfilled by the lead contact, Prof. Erik Vesselli (evesselli@units.it).

Materials availability

This study did not generate new unique reagents, and all experimental information is reported here and is also available upon reasonable request to the lead contact.

Data and code availability

All data and code supporting the findings of this study are available within the article and are described in the supplemental information, can be downloaded for free from the Quantum Espresso repository, or are available from the corresponding author upon reasonable request.

Sample preparation

We started from a Gr/Ir(111) sample prepared *ex situ* following established recipes *in vacuo*[36]: the Ir(111) surface was cleaned by standard cycles of Ar$^+$ sputtering (E = 2 keV) and annealing @1,300–1,350 K and alternated with treatments in oxygen background in the 330–1,070 K temperature range. Before growing Gr, the sample was finally annealed to 1,300–1,350 K in UHV. Gr was grown by thermal cracking of ethylene dosed from the background *in vacuo*. In detail, after saturation with ethylene at room temperature, the crystal was annealed to 1,000 K. At 1,100 K, ethylene was reintroduced in the background, and the temperature was further increased up to 1,300 K. Temperature cycling (1,300–500–1,300 K) followed, always in ethylene background. The complete Gr growth treatment lasted about 30 min. *In situ*, samples were eventually cleaned by standard cycles of Ar$^+$ sputtering (E = 2 keV) and prolonged annealing @950–970 K, while Gr was regrown by dosing ethylene *in situ* at 950 K, followed by flash to 1,050–1,100 K.

The (Co,Fe)TPyP/Gr/Ir(111) monolayers have been grown *in vacuo* by physical vapor deposition of the molecules on the Gr substrate. Cobalt and iron tetra-pyridyl-porphyrin chlorides (CoTPyPCl = 5,10,15,20-tetra(4-pyridyl)21H,23H-porphyrin Co(III) chloride; FeTPyPCl = 5,10,15,20-tetra(4-pyridyl)21H,23H-porphyrin Fe(III) chloride) were purchased from Frontier Scientific. The molecular source was a heated boron nitride crucible. The deposition time for a monolayer, in the range of 15–40 min, was calibrated either by means of a quartz microbalance or N 1s and C 1s core-level intensity ratio analysis (in XPS) depending on the available technique. In order to remove the residual organic contaminants, the molecules have been kept at 500 K nightlong for proper outgassing. The (Co,Fe)TPyP deposition on Gr/Ir(111)

was done with the sample kept at 500 K (unless otherwise specified) in a residual background pressure of 5×10^{-10} mbar, with a crucible temperature of about 600 K. The chloride ligand, which guarantees the chemical stability of the porphyrin in air, detaches from the molecule in the evaporation process.[9,37]

The Fe atoms have been evaporated on the hot sample (500 K), with the molecular layer already prepared, by means of thermal sublimation from a resistively heated pure iron filament.

Photoelectron and absorption spectroscopies

Both XPS and NEXAFS data were collected at the ALOISA (Advanced Line for Overlayer Interface and Surface Analysis) beamline of the CNR-IOM at the Elettra synchrotron radiation facility in Trieste. The XPS photon energies were set to 514 eV for N 1s, 910 eV for Co $2p_{3/2}$, and 850 eV for Fe $2p_{3/2}$ with a corresponding overall energy resolution of 160 meV (N 1s) and 320 meV (Co, Fe 2p).[38] Photoemission spectra were measured at near-normal emission with the sample at a grazing angle of 4° in nearly p-polarization. NEXAFS spectra have been measured with the sample at a fixed grazing angle of 6° while rotating the surface around the (linearly polarized) photon beam axis in order to switch from transverse magnetic (nearly p-polarization) to transverse electric polarization (s-polarization). Absolute energy calibration of the NEXAFS spectra was obtained by simultaneous measurements of the drain current on the last mirror, where the absorption lines of residuals nitrogen contaminants were calibrated by real-time recording of N_2 gas phase NEXAFS. NEXAFS spectra were finally normalized to the Gr/Ir(111) background (reference spectra) following the protocol already described in the literature.[39] Determination of the angular configuration of selected molecular moieties was obtained from the angular dependence of the corresponding resonance intensities with respect to the polarization direction of the impinging light.

Computational details

DFT calculations were performed with the pseudopotential plane wave code Quantum ESPRESSO[40–42] on CoTPyP and CoTPyP-Fe layers. The two systems were described in periodic boundary conditions with supercells of similar size containing two molecules over a domain of 156C and 150C atoms in the mono- and bimetallic cases, respectively. In order to reduce the computational cost, the Ir(111) substrate was neglected after having verified its weak interaction with Gr. In the monometallic case, the most energetically favorable configuration corresponds to an almost hexagonal arrangement of CoTPyPs rotated by 60° one with respect to the other. In the bimetallic system, the CoTPyPs occupy sites of a rectangular (almost square) lattice but are alternatively rotated by 90° as suggested from a previous study on Au(111).[9] In all cases, the geometry was optimized by energy and force minimization, yielding the best structures as depicted in Figure S2.

Spin-polarized calculations were carried out using the Perdew-Burke-Ernzerhof (PBE) exchange correlation functional within the generalized gradient approximation (GGA) method. Vanderbilt ultra-soft pseudopotentials were employed except for Co and Fe atoms, for which Rappe-Rabe-Kaxiras-Joannopoulos (RRKJ) ultra-soft pseudopotentials were used instead.[43] RRKJ pseudopotentials with full and half core-hole ionization were generated for the simulation of the adsorption spectra and core-level shifts; in particular, for the latter, the projected augmented wave (PAW) framework was employed[44] in order to reconstruct the all-electron wave functions. The Hubbard-U correction[45] was introduced to improve the description of the metal atoms 3d states, with a U parameter of 3.5 eV for Co in order to reproduce the

5.5 eV distance between occupied and unoccupied $3d_z2$ levels reported in the literature[46] and U = 6.4 eV for Fe.[47] van der Waals interactions were also included using the Grimme-D3 approach.[48] We employed plane-waves cutoffs of 60 and 240 Ry for the wave function and the charge density, respectively. Brillouin zone sampling was performed on a Monkhorst-Pack 4 × 2 × 1 k-point grid for self-consistent field (SCF) calculations and on an 8 × 4 × 1 grid for non-SCF (NSCF) ones. The Methfessel-Paxton smearing scheme[48] was used for the occupation of electronic states with a smearing parameter of 0.01 Ry. Geometrical optimization was carried out using Broyden-Fletcher-Goldfarb-Shanno algorithm with energy and force convergence thresholds of $1 \cdot 10^{-6}$ Ry and $1 \cdot 10^{-3}$ a.u., respectively. The calculated equilibrium lattice parameter of Gr is 2.46 Å.

N $1s$ core-level shifts (CLSs) were obtained from total energy differences between SCF calculations in which one N atom at a time was described by a pseudopotential taking into account a full core hole (FCH) in $1s$ state, using the final state approximation.[49]

NEXAFS spectra for different nitrogen atoms were computed using the xspectra.x code in half core hole (HCH) approximation.[50] The Fermi golden rule is adopted to compute the transition amplitudes given by the dipole operator directed along the photon beam polarization; those are evaluated between initial and final Kohn-Sham states. The summation over all possible final states is performed by adopting a recursion method based on the Lanczos algorithm. Realignment of spectra coming from different nitrogen atoms was then made using molecularnexafs.x,[51] which performs a shift based on CLSs.

SUPPLEMENTAL INFORMATION

Supplemental information can be found online at https://doi.org/10.1016/j.xcrp.2023.101378.

AUTHOR CONTRIBUTIONS

F.A. and E.V. performed all experiments and data analysis, with P.B., A.A., and D.B. focusing on the NEXAFS and XPS parts, respectively. A.C., A.V., and L.F. took care of the measurements at the beamline. D.B. and M.P. performed the computational part. F.A. and E.V. drafted the paper. F.A., P.B., M.P., and E.V. discussed the interpretation. All authors discussed the results and commented on the manuscript. E.V. coordinated the collaboration.

DECLARATION OF INTERESTS

The authors declare no competing interests.

REFERENCES

1. Whitesides, G.M., and Crabtree, G.W. (2007). Don't forget long-term fundamental research in energy. Science *315*, 796–798. https://doi.org/10.1126/science.1140362.

2. Grohol, M., and Constanze, V.; European Commission (2023). Study on the Critical Raw Materials for the EU. https://doi.org/10.2873/725585.

3. Zhang, L., Ren, Y., Liu, W., Wang, A., and Zhang, T. (2018). Single-atom catalyst: a rising star for green synthesis of fine chemicals. Natl. Sci. Rev. *5*, 653–672. https://doi.org/10.1093/nsr/nwy077.

4. Kaiser, S.K., Chen, Z., Faust Akl, D., Mitchell, S., and Pérez-Ramírez, J. (2020). Single-atom catalysts across the periodic table. Chem. Rev. *120*, 11703–11809. https://doi.org/10.1021/acs.chemrev.0c00576.

5. Gutzler, R., Stepanow, S., Grumelli, D., Lingenfelder, M., and Kern, K. (2015). Mimicking enzymatic active sites on surfaces for energy conversion chemistry. Acc. Chem. Res. *48*, 2132–2139. https://doi.org/10.1021/acs.accounts.5b00172.

6. Haruta, M., Kobayashi, T., Sano, H., and Yamada, N. (1987). Novel gold catalysts for the oxidation of carbon monoxide at a temperature far below 0 °C. Chem. Lett. *16*, 405–408. https://doi.org/10.1246/cl.1987.405.

7. Yang, X.F., Wang, A., Qiao, B., Li, J., Liu, J., and Zhang, T. (2013). Single-atom catalysts: a new frontier in heterogeneous catalysis. Acc. Chem. Res. *46*, 1740–1748. https://doi.org/10.1021/ar300361m.

8. Herzing, A.A., Kiely, C.J., Carley, A.F., Landon, P., and Hutchings, G.J. (2008). Identification of active gold nanoclusters on iron oxide supports for CO oxidation. Science *321*, 1331–1335. https://doi.org/10.1126/science.1159639.

9. Wurster, B., Grumelli, D., Hötger, D., Gutzler, R., and Kern, K. (2016). Driving the oxygen evolution reaction by nonlinear cooperativity in bimetallic coordination catalysts. J. Am. Chem. Soc. *138*, 3623–3626. https://doi.org/10.1021/jacs.5b10484.

10. Hötger, D., Etzkorn, M., Morchutt, C., Wurster, B., Dreiser, J., Stepanow, S., Grumelli, D., Gutzler, R., and Kern, K. (2019). Stability of metallo-porphyrin networks under oxygen reduction and evolution conditions in alkaline media. Phys. Chem. Chem. Phys. *21*, 2587–2594. https://doi.org/10.1039/C8CP07463A.

11. Liu, B., Zhang, S., Miao, G., Guo, J., Meng, S., and Wang, W. (2021). Inspecting the nonbonding and antibonding orbitals in a surface-supported metal-organic framework. Chem. Commun. *57*, 4580–4583. https://doi.org/10.1039/d1cc00506e.

12. Baker Cortés, B.D., Enache, M., Küster, K., Studener, F., Lee, T.L., Marets, N., Bulach, V., Hosseini, M.W., and Stöhr, M. (2021). Structural transformation of surface-confined porphyrin networks by addition of Co atoms. Chemistry *27*, 12430–12436. https://doi.org/10.1002/chem.202101217.

13. Mandal, B., Chung, J.S., and Kang, S.G. (2018). Theoretical insight into M1TPyP-M2 (M1, M2 = Fe, Co) MOFs: correlation between electronic structure and catalytic activity extending to potentiality in capturing flue gases. J. Phys. Chem. C *122*, 9899–9908. https://doi.org/10.1021/acs.jpcc.8b00080.

14. Li, Y., Xiao, J., Shubina, T.E., Chen, M., Shi, Z., Schmid, M., Steinrück, H.P., Gottfried, J.M., and Lin, N. (2012). Coordination and metalation bifunctionality of Cu with 5,10,15,20-tetra(4- pyridyl)porphyrin: toward a mixed-valence two-dimensional coordination network. J. Am. Chem. Soc. *134*, 6401–6408. https://doi.org/10.1021/ja300593w.

15. Gottfried, J.M. (2015). Surface chemistry of porphyrins and phthalocyanines. Surf. Sci. Rep. *70*, 259–379. https://doi.org/10.1016/j.surfrep.2015.04.001.

16. Corva, M., Mohamed, F., Tomsic, E., Rinaldi, M., Cepek, C., Seriani, N., Peressi, M., and Vesselli, E. (2019). Learning from nature: charge transfer and carbon dioxide activation at single, biomimetic Fe sites in tetrapyrroles on graphene. J. Phys. Chem. C *123*, 3916–3922. https://doi.org/10.1021/acs.jpcc.8b11871.

17. Armillotta, F., Pividori, A., Stredansky, M., Seriani, N., and Vesselli, E. (2020). Dioxygen at biomimetic single metal-atom sites: stabilization or activation? The case of CoTPyP/Au(111). Top. Catal. *63*, 1585–1595. https://doi.org/10.1007/s11244-020-01333-9.

18. Hieringer, W., Flechtner, K., Kretschmann, A., Seufert, K., Auwärter, W., Barth, J.V., Görling, A., Steinrück, H.P., and Gottfried, J.M. (2011). The surface trans effect: influence of axial ligands on the surface chemical bonds of adsorbed metalloporphyrins. J. Am. Chem. Soc. *133*, 6206–6222. https://doi.org/10.1021/ja1093502.

19. Corva, M., Ferrari, A., Rinaldi, M., Feng, Z., Roiaz, M., Rameshan, C., Rupprechter, G., Costantini, I., Dell'Angela, M., Pastore, G., et al. (2018). Vibrational fingerprint of localized excitons in a two-dimensional metal-organic crystal. Nat. Commun. *9*, 4703. https://doi.org/10.1038/s41467-018-07190-1.

20. Armillotta, F., Bidoggia, D., Baronio, S., Biasin, P., Annese, A., Scardamaglia, M., Zhu, S., Bozzini, B., Modesti, S., Peressi, M., and Vesselli, E. (2022). Single metal atom catalysts and ORR: H-bonding, solvation, and the elusive hydroperoxyl intermediate. ACS Catal. *12*, 7950–7959. https://doi.org/10.1021/acscatal.2c02029.

21. Vesselli, E. (2020). Tetrapyrroles at near-ambient pressure: porphyrins and phthalocyanines beyond the pressure gap. J. Phys. Mater. *3*, 022002. https://doi.org/10.1088/2515-7639/ab7ab2.

22. Larciprete, R., Ulstrup, S., Lacovig, P., Dalmiglio, M., Bianchi, M., Mazzola, F., Hornekær, L., Orlando, F., Baraldi, A., Hofmann, P., and Lizzit, S. (2012). Oxygen switching of the epitaxial graphene-metal interaction. ACS Nano *6*, 9551–9558. https://doi.org/10.1021/nn302729j.

23. Stöhr, J. (1992). NEXAFS Spectroscopy (Springer-Verlag Berlin Heidelberg).

24. De Jong, M.P., Friedlein, R., Sorensen, S.L., Öhrwall, G., Osikowicz, W., Tengsted, C., Jönsson, S.K.M., Fahlman, M., and Salaneck, W.R. (2005). Orbital-specific dynamic charge transfer from Fe(II)-tetraphenylporphyrin molecules to molybdenum disulfide substrates. Phys. Rev. B *72*. 035448-8. https://doi.org/10.1103/PhysRevB.72.035448.

25. Kolczewski, C., Püttner, R., Plashkevych, O., Ågren, H., Staemmler, V., Martins, M., Snell, G., Schlachter, A.S., Sant'Anna, M., Kaindl, G., and Pettersson, L.G.M. (2001). Detailed study of pyridine at the C 1s and N 1s ionization thresholds: the influence of the vibrational fine structure. J. Chem. Phys. *115*, 6426–6437. https://doi.org/10.1063/1.1397797.

26. Marshall-Roth, T., Libretto, N.J., Wrobel, A.T., Anderton, K.J., Pegis, M.L., Ricke, N.D., Voorhis, T.V., Miller, J.T., and Surendranath, Y. (2020). A pyridinic Fe-N4 macrocycle models the active sites in Fe/N-doped carbon electrocatalysts. Nat. Commun. *11*, 5283–5314. https://doi.org/10.1038/s41467-020-18969-6.

27. Mette, G., Sutter, D., Gurdal, Y., Schnidrig, S., Probst, B., Iannuzzi, M., Hutter, J., Alberto, R., and Osterwalder, J. (2016). From porphyrins to pyrphyrins: adsorption study and metalation of a molecular catalyst on Au(111). Nanoscale *8*, 7958–7968. https://doi.org/10.1039/c5nr08953k.

28. Bai, Y., Sekita, M., Schmid, M., Bischof, T., Steinrück, H.P., and Gottfried, J.M. (2010). Interfacial coordination interactions studied on cobalt octaethylporphyrin and cobalt tetraphenylporphyrin monolayers on Au(111). Phys. Chem. Chem. Phys. *12*, 4336–4344. https://doi.org/10.1039/b924974p.

29. Bai, Y. (2010). Photoelectron Spectroscopic Investigations of Porphyrins and Phthalocyanines on Ag (111) and Au (111): Adsorption and Reactivity.

30. Gunnarsson, O., and Schönhammer, K. (1978). CO on Cu(100)—explanation of the three-peak structure in the X-ray-photoemission-spectroscopy core spectrum. Phys. Rev. Lett. *41*, 1608–1612. https://doi.org/10.1103/PhysRevLett.41.1608.

31. Flechtner, K., Kretschmann, A., Steinrück, H.P., and Gottfried, J.M. (2007). NO-induced reversible switching of the electronic interaction between a porphyrin-coordinated cobalt ion and a silver surface. J. Am. Chem. Soc. *129*, 12110–12111. https://doi.org/10.1021/ja0756725.

32. Isvoranu, C., Wang, B., Schulte, K., Ataman, E., Knudsen, J., Andersen, J.N., Bocquet, M.L., and Schnadt, J. (2010). Tuning the spin state of iron phthalocyanine by ligand adsorption. J. Phys. Condens. Matter *22*, 472002–472024. https://doi.org/10.1088/0953-8984/22/47/472002.

33. Iancu, V., Schouteden, K., Li, Z., and Van Haesendonck, C. (2016). Electron–phonon coupling in engineered magnetic molecules. Chem. Commun. *52*, 11359–11362. https://doi.org/10.1039/c6cc03847f.

34. Scardamaglia, M., Susi, T., Struzzi, C., Snyders, R., Di Santo, G., Petaccia, L., and Bittencourt, C. (2017). Spectroscopic observation of oxygen

dissociation on nitrogen-doped graphene. Sci. Rep. 7, 7960. https://doi.org/10.1038/s41598-017-08651-1.

35. Pan, F., Deng, W., Justiniano, C., and Li, Y. (2018). Identification of champion transition metals centers in metal and nitrogen-codoped carbon catalysts for CO2 reduction. Appl. Catal. B Environ. 226, 463–472. https://doi.org/10.1016/j.apcatb.2018.01.001.

36. Hattab, H., N'Diaye, a.T., Wall, D., Jnawali, G., Coraux, J., Busse, C., van Gastel, R., Poelsema, B., Michely, T., Meyer zu Heringdorf, F.-J., and Horn-von Hoegen, M. (2011). Growth temperature dependent graphene alignment on Ir(111). Appl. Phys. Lett. 98, 141903. https://doi.org/10.1063/1.3548546.

37. Murphy, B.E., Krasnikov, S.A., Sergeeva, N.N., Cafolla, A.A., Preobrajenski, A.B., Chaika, A.N., Lübben, O., and Shvets, I.V. (2014). Homolytic cleavage of molecular oxygen by manganese porphyrins supported on Ag(111). ACS Nano 8, 5190–5198. https://doi.org/10.1021/nn501240j.

38. Floreano, L., Naletto, G., Cvetko, D., Gotter, R., Malvezzi, M., Marassi, L., Morgante, A., Santaniello, A., Verdini, A., Tommasini, F., and Tondello, G. (1999). Performance of the grating-crystal monochromator of the ALOISA beamline at the Elettra Synchrotron. Rev. Sci. Instrum. 70, 3855–3864. https://doi.org/10.1063/1.1150001.

39. Floreano, L., Cossaro, A., Gotter, R., Verdini, A., Bavdek, G., Evangelista, F., Ruocco, A., Morgante, A., and Cvetko, D. (2008). Periodic arrays of Cu-Phthalocyanine chains on Au(110). J. Phys. Chem. C 112, 10794–10802. https://doi.org/10.1021/jp711140e.

40. Giannozzi, P., Baroni, S., Bonini, N., Calandra, M., Car, R., Cavazzoni, C., Ceresoli, D., Chiarotti, G.L., Cococcioni, M., Dabo, I., et al. (2009). Quantum ESPRESSO: a modular and open-source software project for quantum simulations of materials. J. Phys. Condens. Matter 21, 395502. https://doi.org/10.1088/0953-8984/21/39/395502.

41. Giannozzi, P., Andreussi, O., Brumme, T., Bunau, O., Buongiorno Nardelli, M., Calandra, M., Car, R., Cavazzoni, C., Ceresoli, D., Cococcioni, M., et al. (2017). Advanced capabilities for materials modelling with Quantum ESPRESSO. J. Phys. Condens. Matter 29, 465901. https://doi.org/10.1088/1361-648X/aa8f79.

42. Giannozzi, P., Baseggio, O., Bonfà, P., Brunato, D., Car, R., Carnimeo, I., Cavazzoni, C., de Gironcoli, S., Delugas, P., Ferrari Ruffino, F., et al. (2020). Quantum ESPRESSO toward the exascale. J. Chem. Phys. 152, 154105. https://doi.org/10.1063/5.0005082.

43. Rappe, A.M., Rabe, K.M., Kaxiras, E., and Joannopoulos, J.D. (1990). Optimized pseudopotentials. Phys. Rev. B Condens. Matter 41, 1227–1230. https://doi.org/10.1103/PhysRevB.41.1227.

44. Abidin, A.F.Z., and Hamada, I. (2022). Comparative density functional theory study for predicting oxygen reduction activity of single-atom catalyst. Surf. Sci. 724, 122144. https://doi.org/10.1016/j.susc.2022.122144.

45. Cococcioni, M., and de Gironcoli, S. (2005). Linear response approach to the calculation of the effective interaction parameters in the LDA+U method. Phys. Rev. B 71, 035105. https://doi.org/10.1103/PhysRevB.71.035105.

46. Dias da Silva, L.G.G.V., Tiago, M.L., Ulloa, S.E., Reboredo, F.A., and Dagotto, E. (2009). Many-body electronic structure and Kondo properties of cobalt-porphyrin molecules. Phys. Rev. B 80, 155443. https://doi.org/10.1103/PhysRevB.80.155443.

47. Wu, H.C., Li, S.H., and Lin, S.W. (2012). Effect of Fe concentration on Fe-doped anatase TiO2 from GGA + U calculations. Int. J. Photoenergy 2012, 1–6. https://doi.org/10.1155/2012/823498.

48. Methfessel, M., and Paxton, A.T. (1989). High-precision sampling for Brillouin-zone integration in metals. Phys. Rev. B Condens. Matter 40, 3616–3621. https://doi.org/10.1103/PhysRevB.40.3616.

49. Pehlke, E., and Scheffler, M. (1993). Evidence for site-sensitive screening of core holes at the Si and Ge (001) surface. Phys. Rev. Lett. 71, 2338–2341. https://doi.org/10.1103/PhysRevLett.71.2338.

50. Triguero, L., Pettersson, L.G.M., and Ågren, H. (1998). Calculations of near-edge x-ray-absorption spectra of gas-phase and chemisorbed molecules by means of density-functional and transition-potential theory. Phys. Rev. B 58, 8097–8110. https://doi.org/10.1103/PhysRevB.58.8097.

51. Fratesi, G., Lanzilotto, V., Floreano, L., and Brivio, G.P. (2013). Azimuthal Dichroism in near-edge X-ray absorption fine structure spectra of planar molecules. J. Phys. Chem. C 117, 6632–6638. https://doi.org/10.1021/jp312569q.

Supplemental information

Spectroscopic fingerprints

of iron-coordinated cobalt

and iron porphyrin layers on graphene

Francesco Armillotta, Davide Bidoggia, Pietro Biasin, Antonio Annese, Albano Cossaro, Alberto Verdini, Luca Floreano, Maria Peressi, and Erik Vesselli

Supplemental information

	CoTPyP		CoTPyPFe		FeTPyP		FeTPyPFe	
	Value	σ	Value	σ	Value	σ	Value	σ
Γ_1	0.27		0.27		0.27		0.27	
G_1	0.74	0.01	0.67	0.03	0.61	0.02	0.74	0.04
I_1	0.79	0.01	0.53	0.01	0.53	0.003	0.34	0.02
BE_1	398.82	0.002	399.03	0.01	398.48	0.01	398.95	0.02
Γ_2	0.27		0.27		0.27		0.27	
G_2	0.74	0.01	0.67	0.03	0.61	0.02	0.74	0.04
I_2	0.79	0.01	0.53	0.01	0.53	0.003	0.34	0.02
BE_2	399.10		399.43	0.02	398.94	0.01	399.49	0.02
Γ_3	0.27		0.27		0.27		0.27	
G_3	2.10		2.10		1.34		1.34	0.14
I_3	0.21	0.01	0.53	0.02	0.06	0.01	0.30	0.04
BE_3	400.31	0.08	400.28	0.04	399.96		400.43	0.07

Table S1: Best fit parameters of the XPS N 1*s* core level (related to Fig. 2). Γ: Lorentzian width (eV); G: Gaussian width (eV); A: Amplitude (arb. units); BE: Binding Energy (eV). Asymmetry is always set to zero. When the standard deviation (σ) is missing, it means that the parameter has been locked to a specific value. Subscripts 1 and 2 refer to iminic and pyridinic N species, respectively, and 3 to non-adiabatic features.

	CoTPyP	CoTPyPFe
FWHM	1.8	2.3
A_1	0.33	0.48
BE_1	780.1	780.7
FWHM	2.9	2.3
A_2	0.3	0.36
BE_2	782.2	782.8
FWHM	1.8	2.3
A_{GS}	0.15	0.13
BE_{GS}	778.9	778.9

Table S2: Best fit parameters of the Co 2$p_{3/2}$ core level for CoTPyP and CoTPyPFe (related to Fig. 3A). FWHM: Full Width Half Maximum (eV), A: Amplitude (arb. units), BE: Binding Energy (eV). Asymmetry is always set to zero. Numerical subscripts account for the multiplet splitting and shake up, and GS refers to the Gunnarsson and Schönhammer resonance. The error on binding energy is about 50 meV, and on FWHM and amplitudes is about 10% of the value.

	FeTPyP	CoTPyPFe
FWHM	1.2	4.1
A_1	0.3	0.39
BE_1	709.0	711.4
FWHM	1.2	2.3
A_2	0.16	0.85
BE_2	710.1	714.3
FWHM	2.7	
A_3	0.012	
BE_3	712.4	
FWHM	1.2	2.7
A_{GS}	0.19	0.073
BE_{GS}	707.9	708.2

Table S3: Best fit parameters of the Fe 2$p_{3/2}$ core level for FeTpyP and CoTPyPFe (related to Fig. 3B). FWHM: Full Width Half Maximum (eV), A: Amplitude (arb. units), BE: Binding Energy (eV). Asymmetry is always set to zero. Numerical subscripts account for the multiplet splitting and shake up, and *GS* refers to the Gunnarsson and Schönhammer resonance. Error on binding energy is about 50 meV, on Gaussian widths and amplitudes is about 10% of the value.

	300 K		470 K		550 K		650 K		970 K	
	Value	σ	Value	σ	Value	σ	Value	σ	Value	σ
Γ_1	0.27		0.27		0.27		0.27		0.27	
G_1	0.73	0.07	0.73	0.06	0.72	0.05	0.71	0.30	0.71	0.30
I_1	0.83	0.02	0.79	0.02	0.73	0.02	0.08	0.01	0.01	0.02
BE_1	398.67	0.06	398.80	0.03	398.76	0.03	398.93	0.11	398.82	
Γ_2	0.27		0.27		0.27		0.27		0.27	
G_2	0.73	0.07	0.73	0.06	0.72	0.05	0.71	0.30	0.71	0.30
I_2	0.83	0.02	0.79	0.02	0.73	0.02	0.08	0.01	0.01	0.02
BE_2	398.90	0.12	399.11	0.07	399.13	0.05	399.31	0.23	399.20	0.23
Γ_3	0.27		0.27		0.27		0.27		0.27	
G_3	2.10		2.10		2.10		2.10		2.10	
I_3	0.36	0.02	0.30	0.02	0.34	0.02	0.05	0.02	0.13	0.02
BE_3	399.82	0.09	399.95	0.09	399.95	0.09	400.07	0.09	399.97	0.09
Γ_4	0.27		0.27		0.27		0.27		0.27	
G_4	1.67	0.18	1.67	0.18	1.67	0.18	1.67	0.18	1.67	0.18
I_4	0.00		0.00		0.00		0.03	0.01	0.01	0.01
BE_4	402.02	0.06	402.15	0.06	402.15	0.06	402.28	0.06	402.17	0.06
Γ_5	0.27		0.27		0.27		0.27		0.27	
G_5	1.03	0.14	1.03	0.14	1.03	0.14	1.03	0.14	1.03	0.14
I_5	0.00	0.03	0.00	0.03	0.00	0.03	0.00	0.02	0.25	0.05
BE_5	398.27	0.07	398.40	0.07	398.36	0.07	398.53	0.07	398.40	0.07

Table S4: Best fit parameters of N 1*s* core level spectra of the CoTPyP/Gr/Ir(111) stepwise annealing experiment (related to Fig. 4A). Γ: Lorentzian width (eV); G: Gaussian width (eV); A: Amplitude (arb. units); BE: Binding Energy (eV). Asymmetry is always set to zero. When the standard deviation (σ) is missing, the parameter has been locked to a specific value. Subscripts 1 and 2 refer to iminic and pyridinic N species, respectively, 3 to non-adiabatic shakeup, 4 to graphitic N, and 5 to N atoms strongly interacting with substrate.

	300 K		550 K		600 K		650 K		700 K		970 K	
	Value	σ	Value	σ	Value	σ	Value	σ	Value	σ	Value	σ
Γ_1	0.27		0.27		0.27		0.27		0.27		0.27	
G_1	0.60	0.02	0.61	0.03	0.64	0.05	0.71	0.16	0.71	0.16	0.71	0.16
I_1	0.53	0.01	0.45	0.01	0.27	0.01	0.07	0.01	0.05	0.01	0.00	0.01
BE_1	398.50	0.01	398.62	0.01	398.58	0.02	398.70	0.06	398.70	0.06	398.70	0.06
Γ_2	0.27		0.27		0.27		0.27		0.27		0.27	
G_2	0.60	0.02	0.61	0.03	0.64	0.05	0.71	0.16	0.71	0.16	0.71	0.16
I_2	0.53	0.01	0.45	0.01	0.27	0.01	0.07	0.01	0.05	0.01	0.00	0.01
BE_2	398.96	0.01	399.06	0.01	399.06	0.02	399.18	0.02	399.18	0.02	399.18	0.02
Γ_3	0.27		0.27		0.27		0.27		0.27		0.27	
G_3	1.34		1.34		1.34		1.34		1.34		1.34	
I_3	0.05	0.01	0.13	0.01	0.04	0.01	0.00	0.01	0.01	0.01	0.01	0.01
BE_3	399.98		400.10		400.06		400.18		400.18		400.18	
Γ_4	0.27		0.27		0.27		0.27		0.27		0.27	
G_4	1.00	0.39	1.00	0.39	1.00	0.39	1.00	0.39	1.00	0.39	1.00	0.39
I_4	0.00	0.02	0.00	0.02	0.00	0.02	0.00	0.02	0.04	0.03	0.04	0.03
BE_4	398.20	0.26	398.32	0.26	398.28	0.26	398.40	0.26	398.40	0.26	398.40	0.26

Table S5: Best fit parameters of N 1s core level spectra of the FeTPyP/Gr/Ir(111) stepwise annealing experiment (related to Fig. 4B). Γ: Lorentzian width (eV); G: Gaussian width (eV); A: Amplitude (arb. units); BE: Binding Energy (eV). Asymmetry is always set to zero. When the standard deviation (σ) is missing, the parameter has been locked to a specific value. Subscripts 1 and 2 refer to iminic and pyridinic N species, respectively, 3 to non-adiabatic shakeup, and 4 to N atoms strongly interacting with substrate.
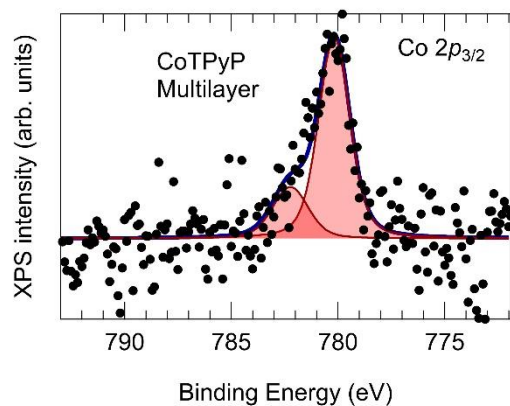
Figure S1: Co 2*p*$_{3/2}$ core level spectrum for the CoTPyP multilayer. Experimental data (dotted curves) are plotted together with its best fit function (solid line) and deconvolution (filled profiles)..
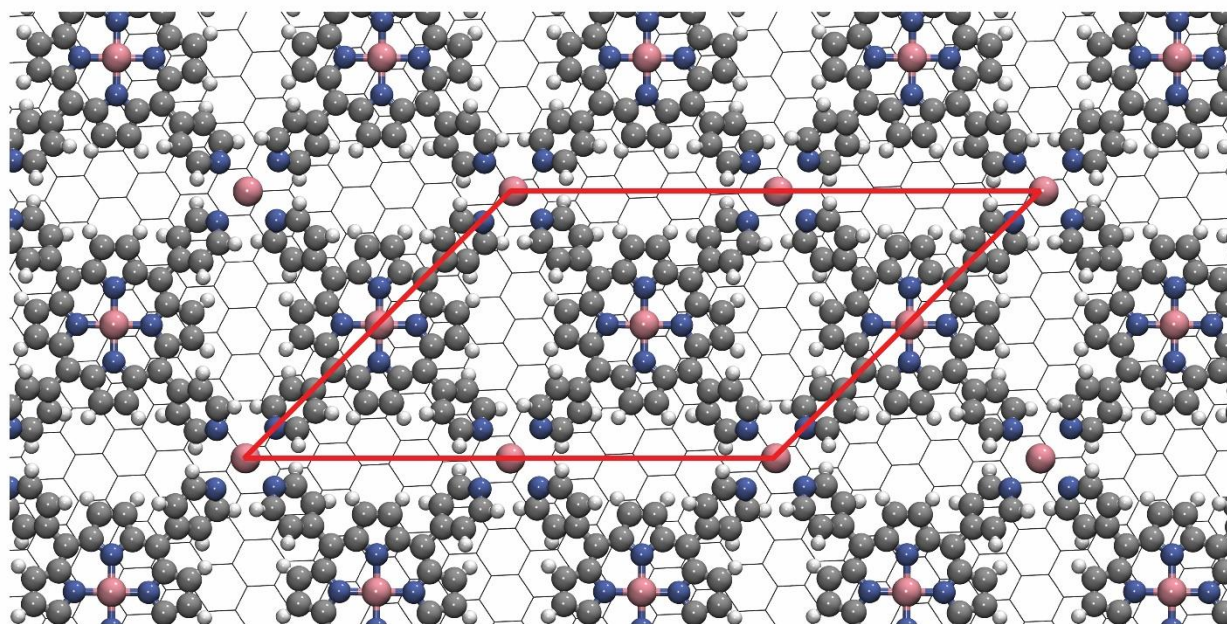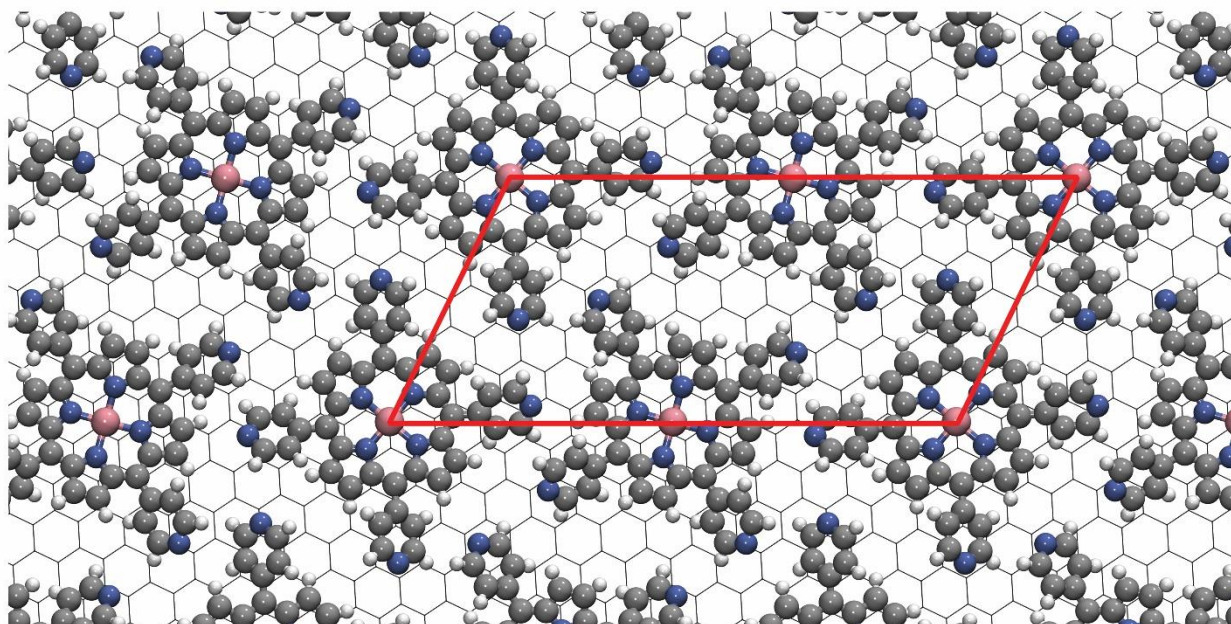
Figure S2. Top views of the computationally optimized structures for the mono- (top) and bi-metallic (bottom) layers on graphene. The unit cells are also depicted (red lines). Color codes: c (gray), N (blue), H (white), and metal (pink).